

Jörg Matthes^{1,*}
Max Kollmer¹
Mark Eberhard²
Veit Hagenmeyer¹
Thomas Kolb^{2,3}


A High-Speed Camera-Based Measurement System for the High-Pressure Entrained-Flow Gasification

A continuously operated optical measurement system for observation and characterization of the flame structure in an entrained-flow gasifier operated at 40 bar and 1200 °C is presented. The experimental setup, the image processing system, and the derived parameters for flame characterization are introduced. First results from gasification experiments concerning flame lift-off distance, flame angle, and flame dynamics are demonstrated.

Keywords: Entrained-flow gasification, Flame monitoring, High pressure, Image processing

Received: September 09, 2022; *revised:* October 23, 2022; *accepted:* October 26, 2022

DOI: 10.1002/ceat.202200434

 This is an open access article under the terms of the Creative Commons Attribution-NonCommercial-NoDerivs License, which permits use and distribution in any medium, provided the original work is properly cited, the use is non-commercial and no modifications or adaptations are made.

1 Introduction

High-pressure entrained-flow gasifiers (EFGs) produce synthesis gas with high quality from fossil and biomass-based feedstocks [1]. In the bioliq[®] process, developed at the Karlsruhe Institute of Technology (KIT) for the production of synthetic fuels from dry biomass residues, a high-pressure EFG converts a suspension fuel produced from biogenic residues in a fast pyrolysis step into a synthesis gas for the subsequent synthesis steps [2, 3]. The feedstock is being extended to plastic waste-based pyrolysis oils.

Flame stability is a major issue for the operation of EFGs with waste-derived fuels. These are by nature characterized by fluctuating specification, i.e., they may vary in calorific value, viscosity, and solid particle content, all affecting flame stability, flame shape, and flame volume. In order to assure stable flame operation, EFGs fed with waste-based fuels are typically operated with a natural gas or fuel oil-fed pilot flame. The need for this auxiliary fuel, which is unfavorable for process efficiency and economics, can be minimized if the operator has a tool to directly assess flame stability during operation. An on-line monitoring is of high value for operation with fluctuating fuel specification, but also for optimization of burner design, e.g., for scale-up or new fuels.

In order to monitor flame structure as a function of fuel specification and operational parameters, e.g., gas-to-liquid ratio (GLR) for atomization, overall stoichiometry of the gasification process as well as steam-to-fuel ratio, an optical measurement system with a high-speed camera has been developed and operated during numerous test runs of the EFG.

In [4], an EFG at KIT is described which is operated under atmospheric pressure with optical access. A high-speed camera is used to take images at different distances from the burner to generate a composite image of the flame that allows qualitative statements on jet breakup and droplet formation. In [5], an optical measurement system for the analysis of the ignition behavior of powdered fuels is presented. Due to the atmospheric

pressure in the furnace, the use of an inspection window as optical access for a high-speed camera is possible. For the analysis of the ignition behavior, the distance between burner nozzle and flame base (lift-off) is determined for different fuels. For this purpose, the camera images are binarized via the Otsu thresholding method, i.e., segmented into flame and background pixels. By time averaging of the thus determined ignition distances over image sequences taken at 500 fps, representative values for each fuel are obtained. The authors in [6] use a back-lighting photography technique to capture the instantaneous self-pulsated spray and stable spray images with a high-speed camera of liquid-centered swirl coaxial injectors.

In [7], optical measurements are reported on an EFG with an operating pressure of 15 bar and an operating temperature of 1400 °C. By design, the operating pressure allows inspection windows in the reactor as optical access. The aim of the optical measurements is to detect the chemiluminescence radiation in the UV range. For this purpose, a special measurement system is presented that uses a CCD camera and a filter wheel with six different optical filters to allow the subtraction of broadband Planck radiation and thus the extraction and analysis of chemiluminescence radiation in the UV.

¹apl. Prof. Dr.-Ing. Jörg Matthes, Max Kollmer, Prof. Dr.-Ing. Veit Hagenmeyer

(joerg.matthes@kit.edu)
Institute of Technology (KIT), Institute for Automation and Applied Informatics (IAI), Hermann-von-Helmholtz-Platz 1, 76344 Eggenstein-Leopoldshafen, Germany.

²Mark Eberhard, Prof. Dr.-Ing. Thomas Kolb
Karlsruhe Institute of Technology (KIT), Institute for Technical Chemistry (ITC), Hermann-von-Helmholtz-Platz 1, 76344 Eggenstein-Leopoldshafen, Germany.

³Prof. Dr.-Ing. Thomas Kolb
Karlsruhe Institute of Technology (KIT), Engler-Bunte-Institut (EBI), Engler-Bunte-Ring 1, 76131 Karlsruhe, Germany.

In [8], an optical measurement system for studying the deposition of macroscopic particles in an EFG for coal gasification is presented. The measurement system has two high-temperature endoscopes (one with straight-on view 0° , one with oblique view 90°) that are inserted into the EFG and to which various camera systems can be connected outside the gasifier. The reactor is operated at temperatures up to about 1500°C . No information is given about the process pressure.

In [9], the authors describe the experimental study on the atomization and particle evolution characteristics in an impinging EFG with coal water slurry. With image processing and statistical methods the particle size distribution after atomization is obtained as well as the spray angle and breakup length. In [10], the particle motion and evolution characteristics in the impinging-flow zone of an impinging entrained-flow gasifier are studied using a visualization system.

The measurement systems presented in literature mainly use inspection windows, which provide access for commercially available optical measurement technology at the low operating pressures and temperatures of the EFGs used. These measurement systems cannot be employed in large-scale EFGs such as those in the *bioliq*[®] plant at operating pressures of up to 80 bar and temperatures of up to 1500°C . In particular, methods with backlighting and multiple optical access points are not feasible there.

In the patent [11], a device for video diagnostics in pressurized gasification reactors is described. The patent uses an endoscope optics, as well as a special pressure and cooling probe, which contains the endoscope as well as the camera system. The system was operated at a POX-system in Freiberg (Germany) with natural gas as feedstock. Successful operation in an EFG using liquid or solid fuel has not been reported.

In contrast to the optical measuring systems known from the literature, the measuring system presented in this paper allows the use under high-pressure conditions up to 80 bar and at high temperatures up to 1500°C for the application of liquid and solid fuels. Here, optical access via inspection windows is no longer possible. Different image processing methods are described that provide characteristic parameters for flame characterization. Results from gasification experiments with variable process parameters are reported.

2 Camera System

The camera system consists of a water-cooled probe installed at an angle of 25° to the vertical burner axis at the reactor top (see Fig. 1). A pressure- and heat-resistant nitrogen-purged protection lens installed at the tip of the camera probe allows the operation of the camera and optics inside the probe under atmospheric pressure conditions. If the protection lens breaks, the pressure-resistant camera probe is auto-

matically flushed with nitrogen, preventing hot synthesis gases from escaping the reactor. A high-pressure resistant cable feed-through enables the power supply of the camera, the control of the motor focus as well as the data transmission via Ethernet. Due to an initial strong soiling tendency of the protective lens, a metallic disk was integrated that allows a nitrogen flow mixed with rinsing water to be directed radially onto the lens.

The interior of the camera system consists of an endoscope with a remote-controlled motor focus. A view angle of 45° and an angular aperture of 60° allows for a direct view of the burner tip and the flame. Due to the installation angle of the camera optics as well as the viewing angle, there is already an almost perpendicular view onto the flame. Due to the large aperture angle, this results in somewhat larger integral lengths for each pixel for the upper and lower areas of the image. However, these differences are not noticeable in the images and are therefore ignored in the following. Different camera systems in the visual spectral range (VIS), e.g., a high-speed camera or a high-dynamic-range camera, can be mounted on the endoscope. The live camera images are transferred to the control room display and can be recorded for analysis.

The used high-speed camera "Sprinter" from Optronis [12] delivers monochrome images (gray scale images with 8 bit resolution). With the used frame size of 896×800 pixels, recordings with a frame rate of 3500 fps are possible. For all experiments, images were taken at the six exposure times of 12, 30, 40, 50, 70, and $125\ \mu\text{s}$. An exemplary raw image is shown in Fig. 2 left. The burner tip is located in the center of the top edge of the image.

In the subsequent analysis of the images, it is assumed that the radiation recorded is predominantly black-body (Planck) radiation due to the hot soot particles in the flame. Other radiation effects such as chemiluminescence radiation in the UV

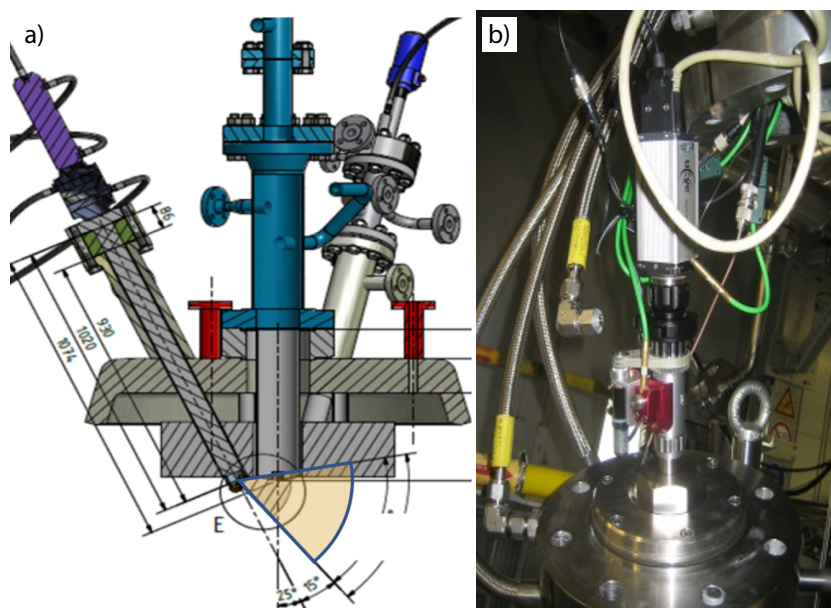


Figure 1. a) Camera probe with field of view (orange) and the multicomponent burner installed at the top of the reactor. b) Interior of the camera system showing the camera, motor focus, and part of the endoscope.

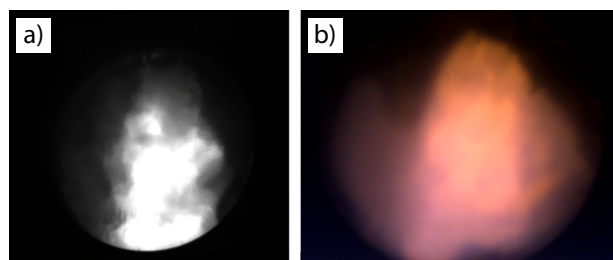


Figure 2. a) Raw image from monochrome high-speed camera at 3500 fps. b) Image from standard RGB camera.

and short-wave VIS (blue, green) are neglected. To validate this assumption, in addition to the monochrome images of the high-speed camera, images were taken with a standard RGB camera μ Eye in the VIS. Fig. 2b gives a representative image. Although additional other radiation effects may also be present, the orange flame color shows that the measured radiation is predominantly Planckian radiation from the soot particles.

3 Image-Processing System

This chapter describes the image processing system for the automated calculation of characteristic flame parameters. For this purpose, the image preprocessing steps are explained in Sect. 3.1 and then the procedures for determining different flame parameters are presented in Sect. 3.2.

3.1 Image Preprocessing

3.1.1 Compensation of Optical Distortion and Geometric Rectification

The aim of the compensation of optical distortion and geometric rectification is to calculate an image with a virtually perpendicular (undistorted) view of the flame. For this purpose, first the optical distortion, mostly barrel distortion, caused by the endoscope optics has to be compensated. For this, a camera model with the intrinsic and extrinsic camera (and optics) parameters is identified via images of a checkerboard pattern at different angles and distances to the camera. By applying the inverse camera model, an optical distortion-minimized image is obtained.

Then, based on an image of the checkerboard pattern at the same distance and angle as the flame is to the camera, a homogeneous transform is determined, which later allows perspective rectification of the flame images. After compensation of optical distortion and geometric rectification, a virtual perpendicular view of the flame with absolute metric information is obtained.

3.1.2 Temporal Mean Image

For the subsequent calculation of the characteristics, a temporal mean image is calculated, which contains the time average

of the gray value from, e.g., 1000 consecutively recorded individual images for each image pixel. With the used framerate of 3500 fps the temporal mean images thus represent the average flame in a time interval of about 0.3 s.

3.1.3 Inverse Abel Transform

For the analysis of the radiation intensity in single volume elements of the flame, an inverse Abel-transform is used, based on the simplifying assumption that the flame is a rotationally symmetric volume radiator. Due to the symmetry requirement, only half the flame image (left or right half) is necessary for the inverse Abel transform. Because of the stronger contamination on the right side of the optics in the images, the temporal mean image of the left half of the image is used here as the basis for the inverse Abel transform in each case. For the computation of the inverse Abel image an implementation described in [13] is applied. Like the original image, the inverse Abel image does not represent absolute physical quantities, but only proportional information about the radiation intensities occurring in the flame. In addition, it should be noted that the inverse Abel transform – like all tomographic methods – is particularly sensitive to disturbances in the original image.

3.2 Flame Parameters

3.2.1 Lift-off Length

The lift-off length of a flame is an important information on flame stability and heat impact to the burner nozzle. A flame sitting on the nozzle will most likely generate a material problem for the burner tip, a stable distance between burner and flame root implies stable operation. A fluctuating distance is a signal for unstable operation and may result in a blow-off of the flame. The flame lift-off is therefore a very valuable information for burner design and gasifier operation, especially for waste-based fuels with potentially inhomogeneous specification.

In order to determine the lift-off length, the average gray value in a small region around the center axis of the flame is calculated for each image row. Fig. 3 shows the gray value curves of the temporal mean images for the acquired exposure times determined in this way. For a better representation, the acquired gray values were normalized with the corresponding exposure times.

One method for determining the lift-off length is to identify the position at which the gray value exceeds a certain threshold in the temporal mean image (cp. Fig. 5). The threshold value can be defined, e.g., relative to the maximum gray value in the respective gray value curve. The authors in [14] discuss this method for an application of direct-injection diesel spray using a relative threshold of 8%. In the images for the EFG flame (cp. Fig. 5), this threshold would still be in the region of low radiant intensity of the flame, presumably caused by reflection and heating processes in the fuel. For this reason, a relative threshold value of 90% is used here (see Fig. 3).

In principle, the relative threshold value can be chosen arbitrarily. Due to the continuous increase of the radiation inten-

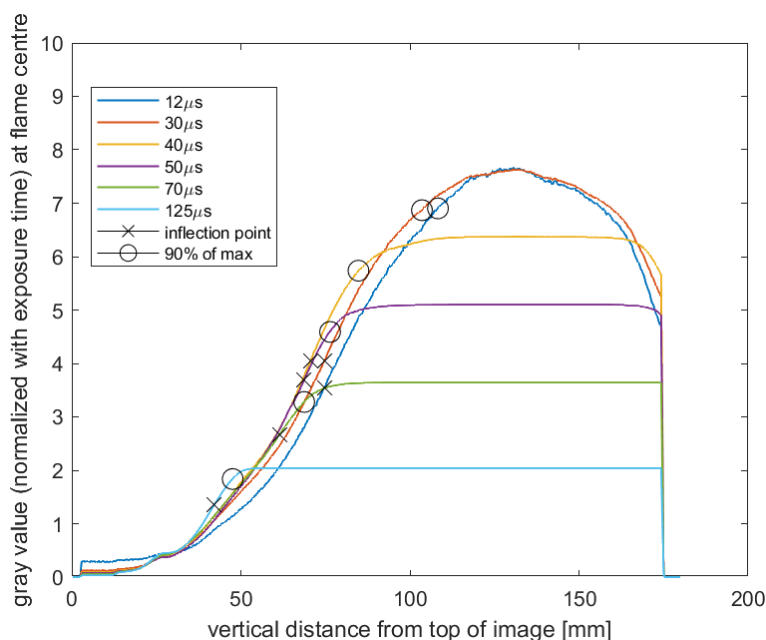


Figure 3. Lift-off length determination with 90 % threshold and inflection point method.

sity, this results in a shift of the determined lift-off length. In the end, the application is not about absolute lengths, but about tracking changes over time. It should be noted, however, that for exposure times at which the saturation of the camera is reached, the relative threshold value ultimately becomes an absolute threshold value, since it then refers to the saturation value (e.g., 255) of the camera. In Fig. 3, the points at which the gray value reaches 90 % of the maximum gray value are depicted as circles. In the example, it can be seen that the values determined for the lift-off distance vary strongly with the relative threshold method.

Another method to determine the lift-off length is to identify the inflection point in the course of the increasing gray value (see crosses in Fig. 3). The idea behind this is that at the point of ignition the radiation intensity increases rapidly. The inflection point can also be sensibly determined for exposure times that lead to saturation of the image sensor. The best results for the inflection point determination were obtained when the first derivative was calculated by numeric backward difference of the gray level gradient in conjunction with a moving average filter for smoothing. The position of the maximum of this derivative then corresponds with the inflection point and thus with the distance from burner to flame. In the example in Fig. 3, the inflection point method provides a significantly smaller variance of the lift-off length compared to the threshold method.

3.2.2 Flame Angle

The flame angle, i.e., the opening angle of the luminous flame at the flame root close to the burner nozzle, is determined by the radial fuel spray distribution (spray angle, droplet size distribution, and velocity) and the aerodynamics of the gas flow emerging the burner quarl. It is a qualitative measure for fuel conversion in the flame, temperature distribution in the reactor, heat impact on the reactor wall, and slag flow. It can be determined based on optical measurements [13, 14]. In the following, two methods for the determination of the flame angle are presented, one based on detecting the flame edge, the other based on the maximum radiant intensity.

3.2.2.1 Flame Angle Based on Flame Edge

When determining the flame angle on the basis of the temporal mean image, the horizontal position of the flame boundary (edge) is first determined for each image row. This is done analogously to the previous section by determining the inflection point of the gray value curve, but now each image row is considered.

Fig. 4 shows exemplarily the gray value progression through an image row (blue). Since here also larger local fluctuations of the gray value can occur in a single image row, a direct numerical determination of the inflection point via smoothing and derivation is not robust enough. For this reason, a curve fit is first performed and the inflection point is then determined using the fitted curve (red in Fig. 4).

For the curve fit the function $g = a_1 \exp[-((x - b_1)/c_1)^2] + a_2 \exp[-((x - b_2)/c_2)^2]$, which represents two superimposed

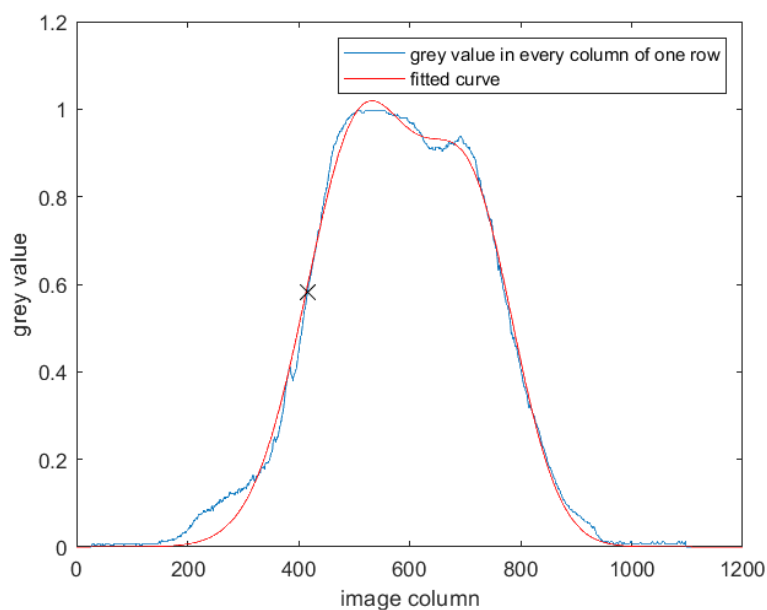


Figure 4. Gray values in a single horizontal image row (blue) and Gauss2 curve fit (red). The cross marks the left inflection point of the fitted curve.

Gaussian functions, is used and the parameters a_1 to c_3 are determined individually for each image row by a least-squares approach. Using the fitted curve, the inflection points at the left and right flame boundaries can be determined.

Due to stronger contamination effects in the right half of the image, only the left half of the flame is used here and for all further evaluations as an example for the characteristic flame parameter calculation. If the limits of the flame are determined for each image row within a defined region of interest (ROI), as shown in Fig. 5a by blue crosses for the left half of the flame, the flame angle can then be determined by a least-squares straight line fit (red in Fig. 5). In the straight line fit, the known position of the burner tip (green in Fig. 5) is explicitly taken into account as a constraint. The flame angle for the considered flame half (here left) is then determined between the fitted straight line and the burner axis (light green in Fig. 5). In

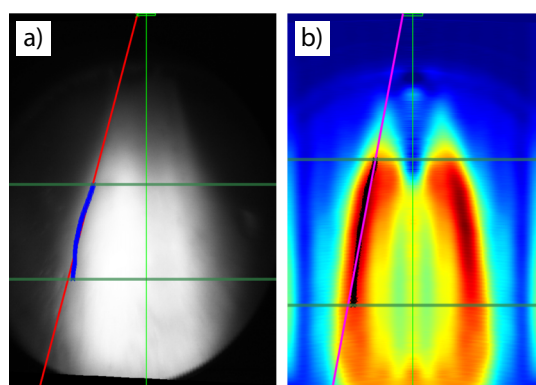


Figure 5. a) Flame borders for each row based on inflection point (blue) and straight line fit (red) for flame angle estimation. Burner tip position and axis are depicted in light green, ROI in dark green. b) Determination of the flame angle based on maximum radiant intensity with inverse Abel image. Black crosses mark points of maximum intensity in each row of the ROI. Burner tip position and axis are depicted in light green, ROI in dark green, straight line fit result in magenta.

general, the flame angle is obtained by adding the left and right angles. In the case, as here, that only one half of the flame is analyzed, the total flame angle is obtained by multiplication with factor 2.

3.2.2 Flame Angle Based on Maximum Radiant Intensity

In the inverse Abel image (see Fig. 5b), the flame zones with the highest radiation intensity can be detected and, based on this, the flame angle between these zones can be determined. For this purpose, the position of maximum intensity is searched for in each image row of the inverse Abel image in the area of a predefined ROI. Analogous to the determination of the flame angle on the basis of the temporal mean image, the positions found are used for a straight line fit.

3.2.3 Analysis of the Flame Size Dynamics

In addition to the steady-state characteristic flame parameters based on the temporal mean image and the inverse Abel image obtained from it, it is also possible to determine parameters that characterize the dynamics of the flame. Their value for technical application has to be investigated in future campaigns.

The fluctuation of the luminosity of the flame, i.e., the time-dependent area of high luminosity detected by the camera, may provide information about the flame dynamics and stability. For this purpose, a constant threshold-based segmentation is first performed in each image of the acquisition sequence into flame and background. Then, the number of pixels occupied by the flame in the current image can be determined.

Fig. 6 illustrates the time course of the flame size over 1 s of recording time. In particular, the smoothed signal (red) shows a low amplitude oscillation at low frequencies (in the example of about 7 Hz). A frequency analysis using fast Fourier transform of the mean-free raw signal confirms this visual impression with a peak at about 7 Hz. Such oscillations can indicate a transition to unstable operation of the burner when the amplitude increases.

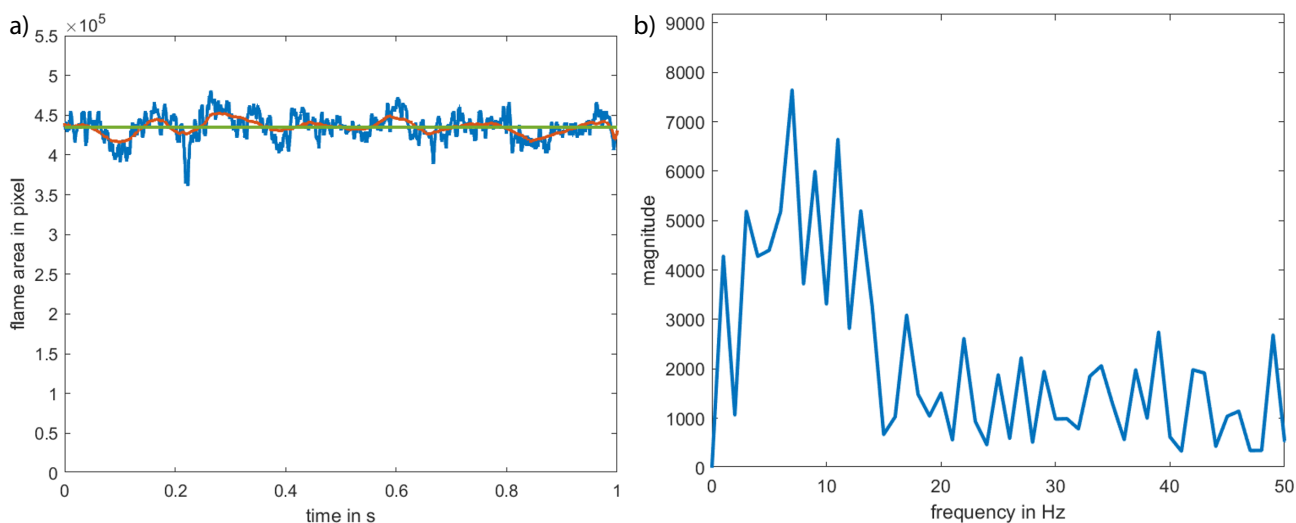


Figure 6. a) Time course of the flame size (blue: raw signal, red: filtered signal). b) corresponding frequency analysis result.

4 Experimental Setup

All test runs for the experimental validation of the methods presented in Sect. 3 were carried out at the KIT-bioliq[®]-EFG described in [2, 3]. The EFG is designed for operating pressures of 40 and 80 bar.

Four different parameter settings were used over a period of about 30 h total. The operational parameters are listed in Tab. 1.

Table 1. Overview of experiment settings.

Setting No.	Fuel input	Stoichiometric ratio λ	Atomizing steam ratio
V107.1	4.5 MW	0.45	100 %
V107.2	4.5 MW	0.45	50 %
V107.3	4.5 MW	0.55	100 %
V107.4	3.5 MW	0.55	75 %
V107.5	4.5 MW	0.45	100 %

Experiment V107.1 and V107.5 have the same settings and are used to test reproducibility. For each of the settings, except for V107.5, two separate measurements were performed with the high-speed camera system at intervals of approx. 1.5 h, which will henceforth be denoted by, e.g., V107.1(1) and V107.1(2). The parameters varied are: (i) fuel load from 4.5 MW (standard load) to 3.5 MW, (ii) stoichiometric ratio from 0.45 to 0.55, and (iii) atomization steam flow from 50 % to 100 %. These variations are within the typical range of operation of the KIT-EFG.

5 Results and Discussion

In this chapter, results of the experimental validation of the methods presented in Sect. 3 for calculating camera-based flame parameters are presented and discussed. On the one hand, the reproducibility of the camera-based flame parameters with the same test settings, but also the significance for varying test parameters will be presented and discussed.

5.1 Lift-off Length

First, the reproducibility of the camera-based lift-off distance measurement is to be investigated. For this purpose, experiments 107.1 and 107.5 are regarded, since they have the same operational settings. The recordings V107.1(1) and V107.1(2) were taken within a 80-min interval, whereas the V107.5(1) recording was taken at the end of the experimental series about 29 h after V107.1.

Tabs. 2 and 3 present the results for settings 107.1(1), 107.1(2), and V107.5(1). For the calculation of the mean values, only the exposure times 30–70 μ s are considered here and in all further investigations, in order to eliminate the outliers that can arise due to underexposure effects with too short exposure times or due to saturation effects with too long exposure times. The so calculated mean values form a reliable basis for further investigations.

The inflection point-based method consistently yields smaller lift-off distances than the method based on a relative threshold of 90 % with respect to the maximum gray value. In principle, it would be possible to adjust the results of the two methods by the choice of the relative threshold. However, the camera-based parameters are primarily intended to reflect relative changes as the experimental parameters change.

If the individual procedures with the different exposure times for experiments 107.1(1), 107.1(2), and 107.5(1) are considered, it can be seen that similar results are obtained in each case and thus reproducibility is given, even after 29 h of operation. It should be mentioned here, however, that the values with different exposure times differ greatly from each other. The results are dependent on the exposure time used. Therefore, as mentioned before, mainly the mean values of the lift-off distances over exposure times 30–70 μ s are considered here. These mean values differ between V107.1(1) and V107.5(1) by only 4 mm for the threshold method and are identical for the inflection point method.

Now it is to be investigated how sensitively the camera-based determined lift-off distances react to changes in the operational settings. For this purpose, the results of the mean values over the exposure times 30–70 μ s for experiments 107.1(1)–107.5(1) listed in Tab. 4 are considered.

The data from Tab. 4 show a remarkable influence of atomization steam ratio on flame lift-off distance (V107.1 vs. V107.2) whereas the careful shift in stoichiometric ratio and fuel load only show minor effects (V107.1 vs. V107.3 and V107.4)

Table 2. Lift-off length for experiments 107.1(1), 107.1(2), and 107.5(1) for different exposure times using the inflection point method.

Exposure time	12 μ s	30 μ s	40 μ s	50 μ s	70 μ s	125 μ s	Mean
V107.1(1)	73 mm	67 mm	71 mm	65 mm	54 mm	42 mm	64 mm
V107.1(2)	84 mm	67 mm	68 mm	61 mm	56 mm	42 mm	63 mm
V107.5(1)	75 mm	75 mm	65 mm	63 mm	51 mm	39 mm	64 mm

Table 3. Lift-off length for experiments 107.1(1), 107.1(2), and 107.5(1) for different exposure times using the 90 % relative threshold method.

Exposure time	12 μ s	30 μ s	40 μ s	50 μ s	70 μ s	125 μ s	Mean
V107.1(1)	95 mm	85 mm	80 mm	70 mm	59 mm	48 mm	74 mm
V107.1(2)	101 mm	84 mm	75 mm	65 mm	52 mm	46 mm	69 mm
V107.5(1)	101 mm	90 mm	69 mm	67 mm	55 mm	42 mm	70 mm

Table 4. Distance burner to flame. Mean values over exposure times 30–70 μs for all operational settings with inflection point as well as relative threshold method.

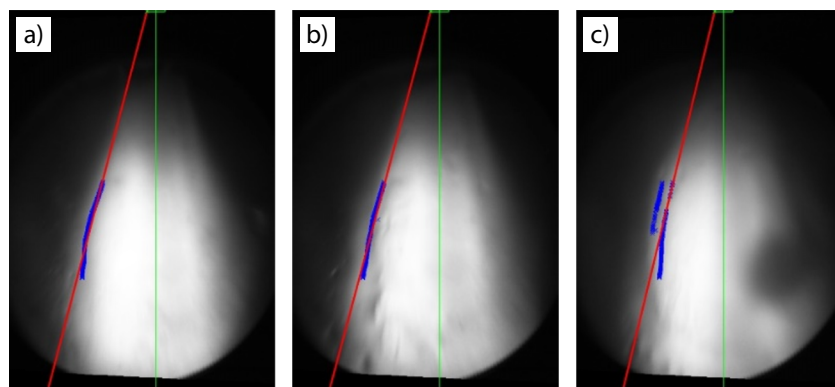
Experiment	Inflection point method	Relative threshold method
V107.1(1)	64 mm	74 mm
V107.2(1)	53 mm	57 mm
V107.3(1)	70 mm	84 mm
V107.4(1)	69 mm	84 mm
V107.5(1)	64 mm	70 mm

5.2 Flame Angle

5.2.1 Flame Angle Based on Flame Edge

First, for the camera-based determined flame angles based on the flame edges, the reproducibility is also to be investigated with initially identical test settings. For the experiments V107.1(1), V107.1(2), and V107.5(1), the average flame images with edge-based flame angles are depicted in Fig. 7. For the calculation of the flame angles based on flame edge, only the left halves of the images are used here.

For the flame angles, the values in Tab. 5 are obtained. Analogous to the camera-based determination of the lift-off distance, there is also a strong dependence of the flame angle on the exposure time used. Therefore, the respective mean angles over exposure times 30–70 μs will be considered as the representative quantity.

**Figure 7.** Average flame images for V107.1(1) (a) and V107.1(2) (b) taken about 80 min apart and for V107.5(1) (c) taken about 29 h after V107.1 for exposure time 30 μs .**Table 5.** Flame angle based on flame edge for experiments 107.1(1), 107.1(2), and 107.5(1) with different exposure times and mean values for 30–70 μs .

Experiment	12 μs	30 μs	40 μs	50 μs	70 μs	125 μs	Mean
V107.1(1)	23.3°	29.4°	29.3°	32.6°	40.0°	47.3°	32.8°
V107.1(2)	23.3°	29.9°	30.5°	35.7°	41.4°	46.3°	34.4°
V107.5(1)	22.0°	27.1°	31.3°	32.5°	36.7°	48.8°	31.9°

A comparison of the images of V107.1(1), V107.1(2), and V107.5(1) yields similar mean flame images as can be seen in Fig. 7. However, the contamination of the camera optics in the right half of the image of 107.5(1) should be noted, which has built up after more than 29 h of testing. This contamination is of no further importance here, since only the left halves of the images are used for the calculations of the flame angles. For the flame angles averaged over the exposure times 30–70 μs , 32.8°, 34.4°, and 31.9° result. This means only small deviations are obtained, which indicate a good reproducibility of the camera-based flame angle determination.

Now the sensitivity of the camera-based measurement of the flame angle with respect to operational settings is considered. Tab. 6 shows the results for all settings. Again the effect of atomization steam ratio is rather pronounced (V107.1 vs. V107.2), whereas the other parameter changes do not influence the flame angle significantly.

Table 6. Mean values of flame angles based on flame edge over exposure times 30–70 μs for all operational settings.

Experiment	Mean
V107.1(1)	32.8°
V107.2(1)	39.2°
V107.3(1)	30.7°
V107.4(1)	26.8°
V107.5(1)	31.9°

5.2.2 Flame Angle Based on Maximum Radiant Intensity

For the flame angle of the maximum radiant intensity, the reproducibility of the parameters is also first investigated with the same experimental settings. The analysis is carried out here on the basis of the images with 12 and 30 μs exposure time. Longer exposure times partly lead to saturation effects of the camera chip and to invalid results of the inverse Abel transform. Thus, here only the recordings with 12 and 30 μs are considered. The obtained flame angles for all operational settings are listed in Tab. 7.

Also the comparison of the experiments V107.1(1) and V107.5(1) with the same experimental settings carried out at intervals of approx. 29 h show acceptable results with 9.8° and 9.7° at 12 μs exposure time and with 18.6° and 21.7° at 30 μs exposure time. However, the results for 12 μs exposure time show larger variations even within the same experimental settings. The results for 30 μs exposure time are better

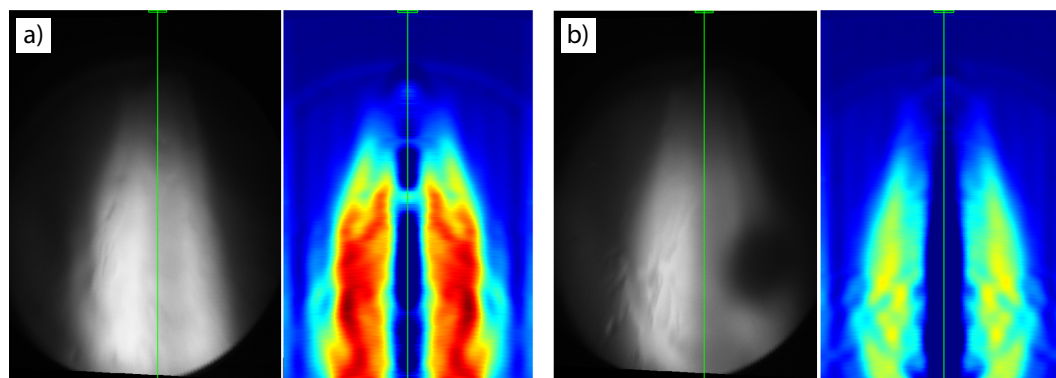
Table 7. Flame angles based on maximum radiant intensity for 12 μs and 30 μs exposure time.

Experiment	12 μs	30 μs
V107.1(1)	9.8°	18.6°
V107.1(2)	12.5°	18.2°
V107.2(1)	13.4°	21.3°
V107.2(2)	8.0°	23.9°
V107.3(1)	12.6°	18.4°
V107.3(2)	18.8°	21.6°
V107.4(1)	7.2°	7.6°
V107.4(2)	10.8°	9.0°
V107.5(1)	9.7°	21.7°

here. The dependency on the exposure time is already a sign that the method is not particularly reliable. Since here for the inverse Abel transform only two exposure times can be used meaningfully, there is hardly any possibility to use mean values over several exposure times as more reliable quantities. Considering the wide range of the obtained flame angles between 7.6° and 23.9°, deviations between the flame angles at the same operational settings of max. 3.2° for V107.3 and on average 1.9° are still acceptable as validation of reproducibility.

Nevertheless, it must be noted that the calculation of the inverse Abel images is very sensitive to disturbances of the captured flame image, e.g., due to contamination of the camera optics. This results in greater uncertainties when determining parameters on the basis of the inverse Abel image.

Fig. 8 displays the inverse Abel images for experiments V107.3(1) and V107.3(2) as well as the corresponding temporal mean images. Only the left half of the mean images is used for inverse Abel transform. Although the corresponding temporal mean images are very similar in the left half at first glance, there are some significant differences in the corresponding inverse Abel images and can thus also lead to differences in the calculated flame angles of the maximum radiant intensity.

**Figure 8.** Temporal mean images and inverse Abel images for experiments V107.3(1) (a) and V107.3(2) (b) for 30 μs exposure time.

5.3 Analysis of the Flame Size Dynamics

Fig. 9 demonstrates the dynamics of the flame size for experiments V107.1(1)–V107.4(1) with 40 μs exposure time. The blue line is the raw signal, the red line a filtered (smoothed) signal, and the green line the mean. In all experiments the flame size is almost constant with a low amplitude and low frequency (below 10 Hz) oscillation. An increase of the oscillation amplitude could be monitored to detect instabilities of the flame at an early stage.

6 Conclusion

A camera-based measurement system with a high-speed camera for automated analysis of flame properties and first experimental results from a research campaign at the KIT EFG are presented. The system is developed for operation under harsh operational conditions (1200 °C, 40 bar). Endoscope optics with an oblique view, a special optics cleaning system, and a pressure- and temperature-resistant, hermetically sealed pressure probe for the camera are the major parts of the system. Stable operation of the camera system with reproducible results was demonstrated over 29 h operation.

Image processing methods are presented which allow an automated calculation of characteristic parameters of the flame. On the basis of a temporal mean image, an estimate of the lift-off distance can be determined using the axial (vertical) gray value curve. The flame lift-off distance can be used to judge flame stability and heat impact to the burner nozzle. In addition, the temporal mean image can be used to calculate the flame angle which is related to the flame length and can be a valuable information on fuel conversion and heat release over the length of the reactor.

Based on a tomographic analysis of the flame radiation by means of an inverse Abel transform, the flame angle based on the zone of maximum radiant intensity in the flame can be determined, alternatively. In addition, parameters characterizing the dynamics of the flame can be calculated. For example, a frequency analysis of the flame size can reveal oscillations that can be an indicator for an unstable flame.

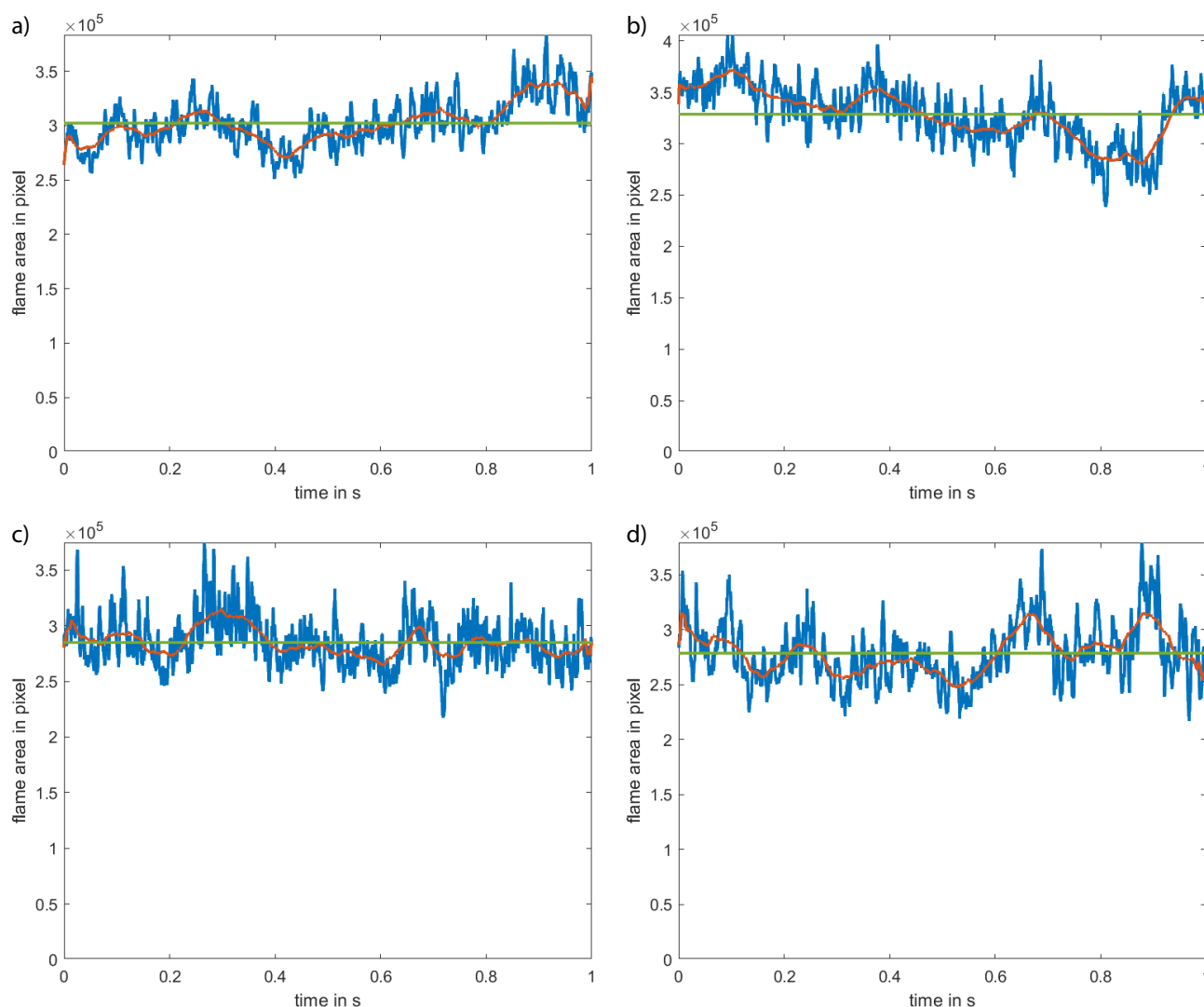


Figure 9. Dynamic of the flame size for experiments V107.1 (a) to V107.4 (d).

The new methods and characteristic parameters are validated on the basis of recordings from a measurement campaign lasting several days on the KIT EFG. The reproducibility of the parameters is demonstrated for the same experimental settings over a period of more than 29 h of operation, especially if averaged values over several recorded exposure times are considered. In addition, changes in the operational parameters of the burner are reflected in the camera-based parameters. Further measurement campaigns are needed to further analyze the correlations between operating parameters of the burner and the camera-based measured characteristics.

Acknowledgment

The authors acknowledge the financial support of the Helmholtz Association of German Research Centres (HGF) within the framework of the Program-Oriented Funding POF IV in the programs “Energy Systems Design (ESD)” and “Materials

and Technologies for the Energy Transition (MTET)”, the Baden-Württemberg State Ministry of Economics, Labor, and Housing for financing the bioliq[®] pilot plant. Thanks are due to our industrial partner Air Liquide Engineering & Construction for financial participation, for building the plant, and for consulting within the framework of the cooperation. Open access funding enabled and organized by Projekt DEAL.

The authors have declared no conflict of interest.

Abbreviations

EFG entrained-flow gasifier
ROI region of interest

References

- [1] *Gasification*, 2nd ed. (Eds: C. Higman, M. van der Burgt), GPP, Burlington, MA **2008**.
- [2] T. Kolb, M. Aigner, R. Kneer, M. Müller, R. Weber, N. Djordjevic, *J. Energy Inst.* **2015**, *89* (4), 485–503. DOI: <https://doi.org/10.1016/j.joei.2015.07.007>
- [3] M. Eberhard, U. Santo, B. Michelfelder, A. Günther, P. Weigand, J. Matthes, P. Waibel, V. Hagenmeyer, T. Kolb, *ChemBioEng Rev.* **2020**, *7* (4), 106–118. DOI: <https://doi.org/10.1002/cite.201700086>
- [4] H. Lu, Y. Gong, X. Wu, Q. Guo, L. Ding, G. Yu, *Fuel* **2022**, *324* (Part B), 124648. DOI: <https://doi.org/10.1016/j.fuel.2022.124648>
- [5] S. Fleck, U. Santo, C. Hotz, T. Jakobs, G. Eckel, M. Mancini, R. Weber, T. Kolb, *Fuel* **2018**, *2017*, 306–319. DOI: <https://doi.org/10.1016/j.fuel.2017.12.077>
- [6] A. C. Sarroza, T. D. Bennet, C. Eastwick, H. Liu, *Fuel Process. Technol.* **2017**, *157*, 1–11. DOI: <https://doi.org/10.1016/j.fuproc.2016.11.002>
- [7] J. Servaites, S. Zelepouga, D. Rue, *Real Time Flame Monitoring of Gasifier Burner and Injectors*, Report, Gas Technology Institute Des Plaines, IL, GTI Project No. 61162, **2003**.
- [8] Y. Gong, G. Yu, Q. Guo, Z. Zhou, F. Wang, Y. Liu, *Chem. Eng. Sci.* **2015**, *138*, 291–302. DOI: <https://doi.org/10.1016/j.ces.2015.08.013>
- [9] L. Gröschel, F. Schäfer, M. Werschy, K.-H. Krause, U. Klotzsche, *Patent DE 44 38 229 C 2*, **1996**.
- [10] www.optronis.com (Accessed on October 18, 2022)
- [11] C. Killer, *Abel Inversion Algorithm*, MATLAB Central File Exchange, retrieved **2022**.
- [12] D. L. Siebers, B. S. Higgins, *Effects of Injector Conditions on the Flame Lift-Off Length of DI Diesel Sprays*, Report, Albuquerque, New Mexico **2000**.
- [13] X. Wu, Y. Gong, Q. Guo, Z. Xue, G. Yu, *Chem. Eng. Sci.* **2019**, *207*, 542–555. DOI: <https://doi.org/10.1016/j.ces.2019.06.055>
- [14] X. Bai, P. Cheng, L. Sheng, Q. Li, X. Zhang, Z. Kang, *Int. J. Multiphase Flow* **2019**, *116*, 239–249. DOI: <https://doi.org/10.1016/j.ijmultiphaseflow.2019.04.017>